Outgassing behaviour during highly explosive basaltic eruptions

Emily C. Bamber [a,b*], Giuseppe La Spina [c,b], Fabio Arzilli [d,b], Margherita Polacci [b], Lucia Mancini [e], Mattia de' Michieli Vitturi [f,g], Daniele Andronico [c], Rosa Anna Corsaro [c] and Mike R. Burton [b]

[a] Department of Earth Sciences, University of Turin, Via Valperga Caluso, 35, 10125, Turin, Italy

[b] Department of Earth and Environmental Sciences, The University of Manchester, Oxford Road, Manchester, M13 9PL, UK

[c] Istituto Nazionale di Geofisica e Vulcanologia - Osservatorio Etneo, Sezione di Catania, Piazza Roma, 2, 95125, Catania, Italy

[d] School of Science and Technology, Geology Division, University of Camerino, Camerino, Italy

[e] Slovenian National Building and Civil Engineering Institute, 1000 Ljubljana, Slovenia

[f] Department of Geology, University at Buffalo, Buffalo, NY 14260, USA

[g] Istituto Nazionale di Geofisica e Vulcanologia, Sezione di Pisa, Via Cesare Battisti, 53, 56125, Pisa, Italy

Sample	Eruption	Unit	Intensity	Mass eruption rate (kg s^{-1})	Eruption column height (km)	Erupted volume (km^3)
FL_AB_1 FL_AB_2	Fontana Lapilli	A/B	Plinian	1.4 x 10^8	32	2.9-3.8
FL_D_1 FL_D_2		D				
FL_E_1 FL_E_2		E				
FL_F_1 FL_F_2		F				
FL_LG_1 FL_LG_2		LG				
MTL1_a0_1 MTL1_a0_2	Masaya Triple Layer	TLL1	Plinian	1 x 10^8	32	3.4
MTL2_a0_1 MTL2_a0_2		TLL2				
MTL3_a0_1 MTL3_a0_2		TLL3				
Etna122_C1_1 Etna122_C3_1	Etna 122 BC	C	Plinian	8.5 x 10^7	26	0.4
Etna2013_1	Etna 2013	23/11/13	Large-scale lava fountain	4.5 x 10^5	11	0.0016
Etna2001_1	Etna 2001	24-31 July	Lava fountain			

Supplementary Table 1: Samples examined by synchrotron-based X-ray microtomography of the Fontana Lapilli (FL) and Masaya Triple Layer (MTL) eruptions of Las Sierras-Masaya volcanic system, and the 122 BC, 2001 and 2013 eruptions of Etna. The key parameters used to classify the eruption intensity are also presented. Data on mass eruption rate, column height and erupted volume were obtained from the following references for each eruption: Fontana Lapilli[1], Masaya Triple Layer[2], Etna 122 BC[3], Etna 2013[4-5]. Eruption parameters for the 2001 eruption are not presented here due to the variations in the eruption rate and erupted volume which occurred during the eruption between July and August 2001.

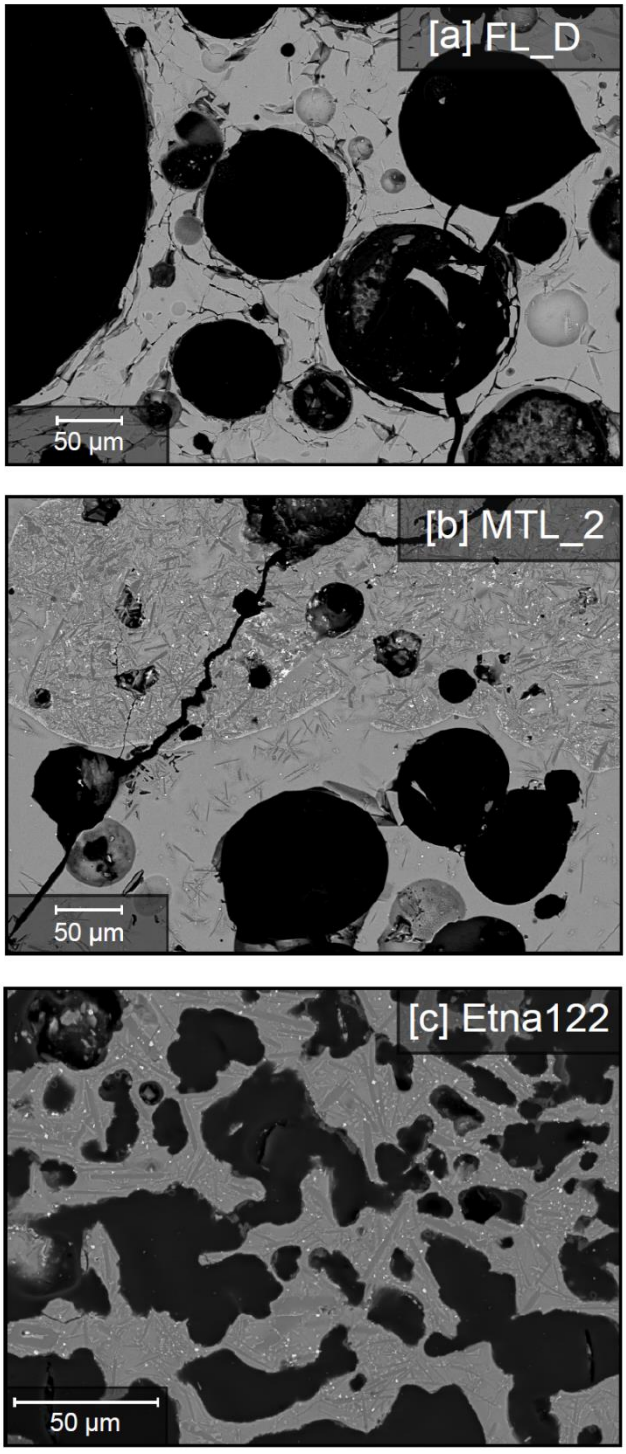

Supplementary Figure 1: Representative back-scattered electron (BSE) images of clasts from each eruption, illustrating the change in vesicle morphology with increasing crystallisation within the matrix. **(a)** Crystal-poor matrix of unit D, Fontana Lapilli eruption. **(b)** Mingled crystal-rich and crystal-poor matrix of TLL2, Masaya Triple Layer eruption, showing the different shape and size of the vesicles between the crystal-poor and crystalline parts of the matrix. **(c)** Crystal-rich matrix of unit C3, Etna 122 BC eruption, showing the most irregular shaped vesicles.

Parameter	Variable	Range	Unit
Bubble number density	N_d	10^9 - 10^{14}	m^{-3}
Tortuosity factor	m	1.01 - 10	
Throat-pore size ratio	f_{tb}	0.03 - 1	
Friction coefficient	f_0	10^{-5} - 1	

Supplementary Table 2: Input ranges used for the sensitivity analysis.

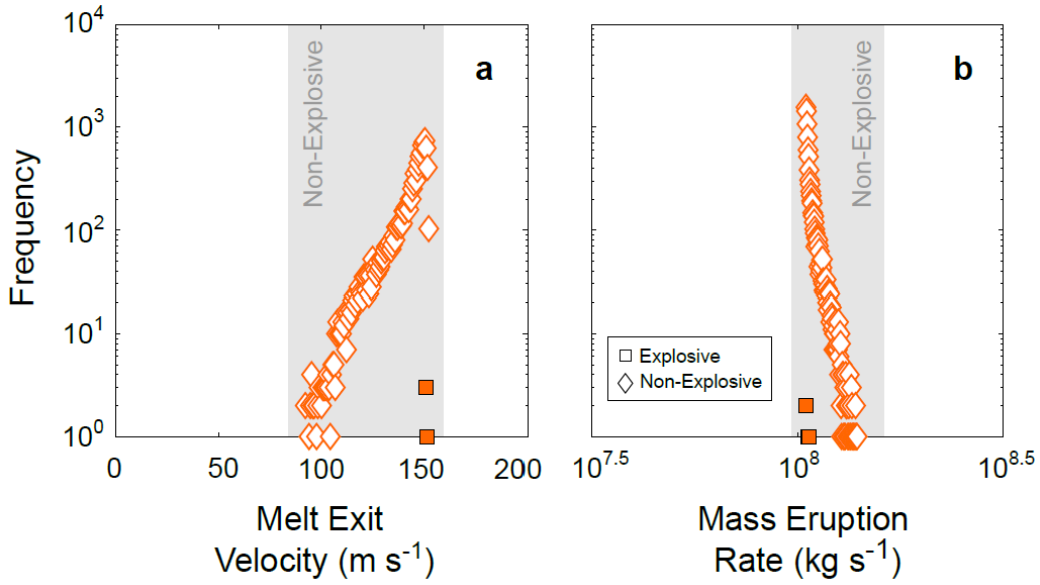

Supplementary Figure 2: Results of the MTL crystal-poor sensitivity analysis, showing the frequency of solutions for the output parameters **(a)** melt exit velocity and **(b)** mass eruption rate. The coloured squares represent explosive solutions and non-explosive solutions are represented by the white diamonds with a coloured outline.

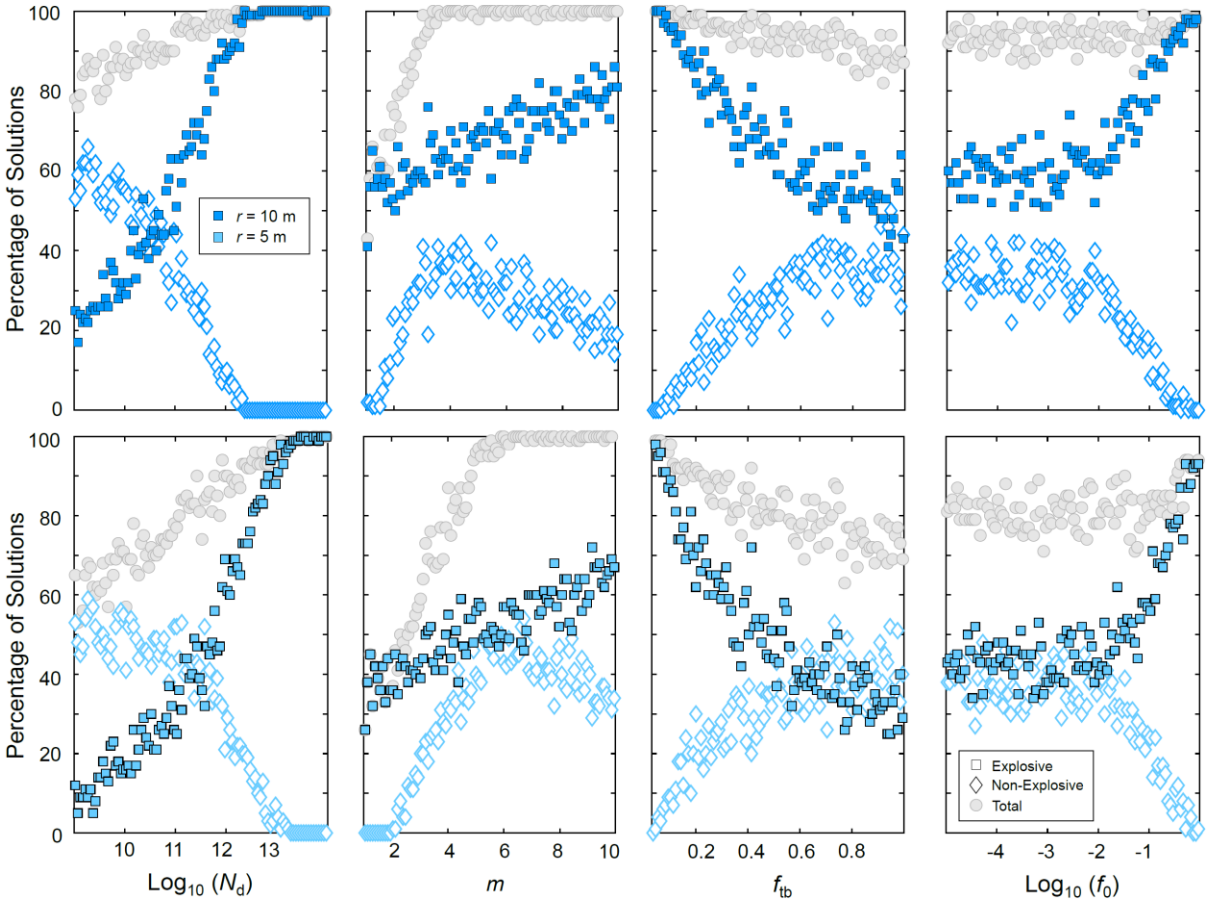

Supplementary Figure 3: Results of the sensitivity analysis for the MTL crystal-rich case, using a conduit radius (r) of 10 m and 5 m.

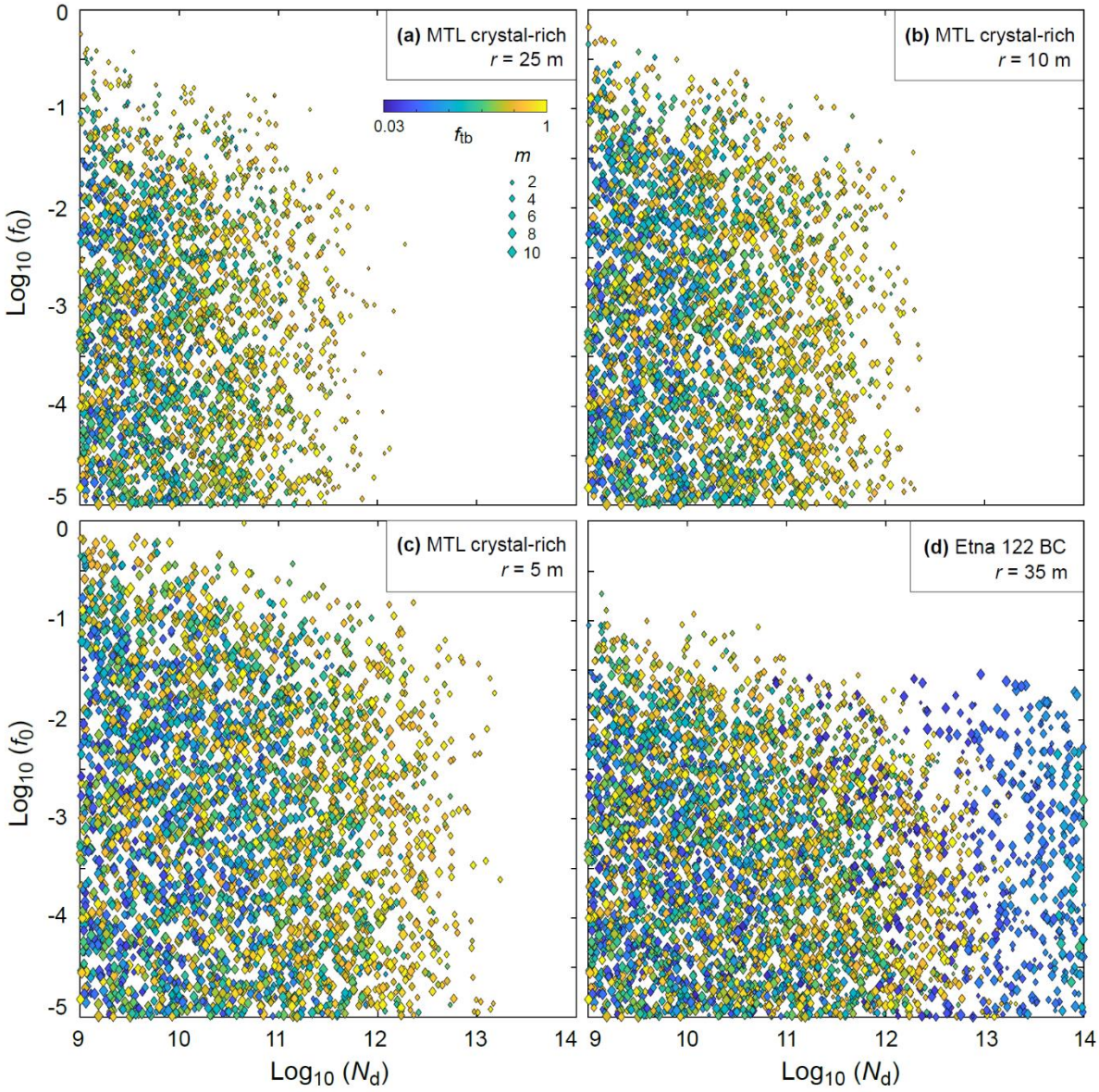

Supplementary Figure 4: Results of the sensitivity analyses, illustrating the relative importance of the Forchheimer parameters (N_d, f_0, f_{tb} and m) on explosivity. Each symbol represents a single solution from the sensitivity analyses and has a value of N_d, f_0, f_{tb} and m used as the initial condition for the simulation. The colour bar represents values of f_{tb} from 0.03 to 1, whilst the size of the symbol scales with m (from 1.01 to 10). Results from the sensitivity analysis using the MTL crystal-rich initial conditions and magma composition, **(a)** for a conduit radius (r) of 25 m, **(b)** for a conduit radius of 10 m and **(c)** for a conduit radius of 5 m. **(d)** Results from the sensitivity analysis using the Etna 122 BC initial conditions and magma composition, for a conduit radius of 35 m. All results represent non-explosive solutions.

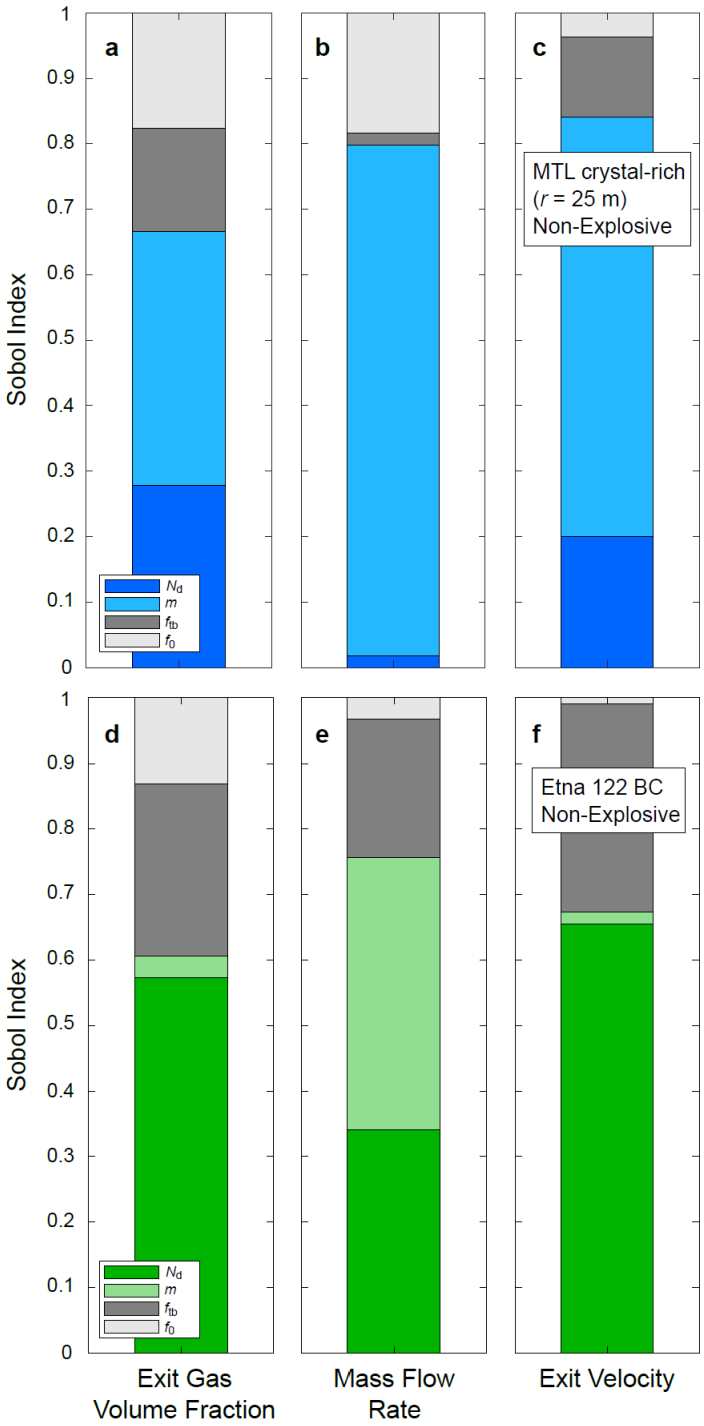

Supplementary Figure 5: Sobol index illustrating the results of the **(a-c)** MTL crystal-rich and **(d-f)** Etna 122 BC sensitivity analyses, showing the control of the input parameters bubble number density (N_d), tortuosity factor (m), throat-pore size ratio (f_{tb}) and the friction coefficient (f_0) on the output parameters for non-explosive solutions.

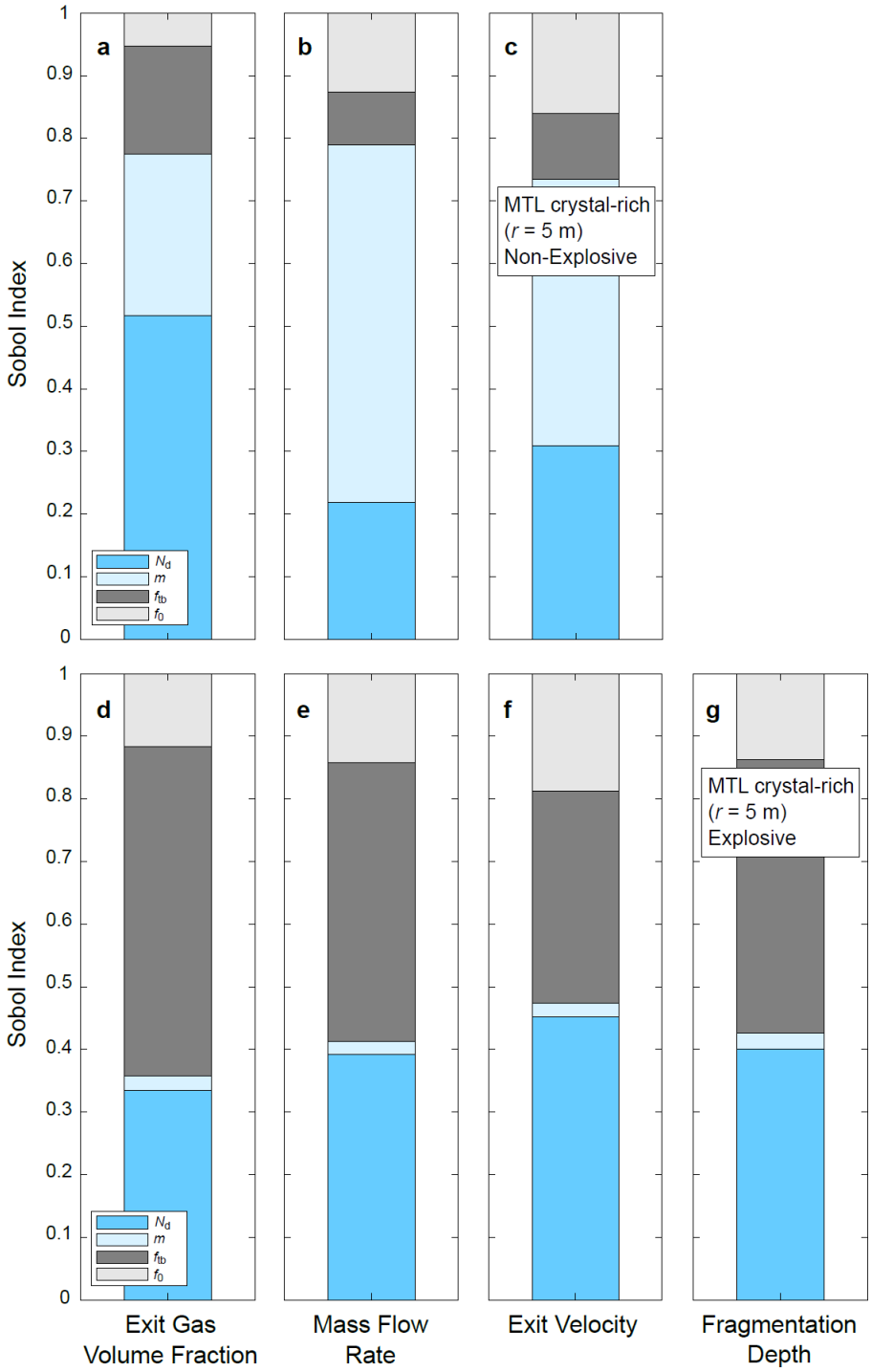

Supplementary Figure 6: Sobol index illustrating the results of the MTL crystal-rich sensitivity analysis using a conduit radius of 5 m, showing the control of the input parameters on the output parameters, for **(a-c)** non-explosive and **(d-g)** explosive solutions.

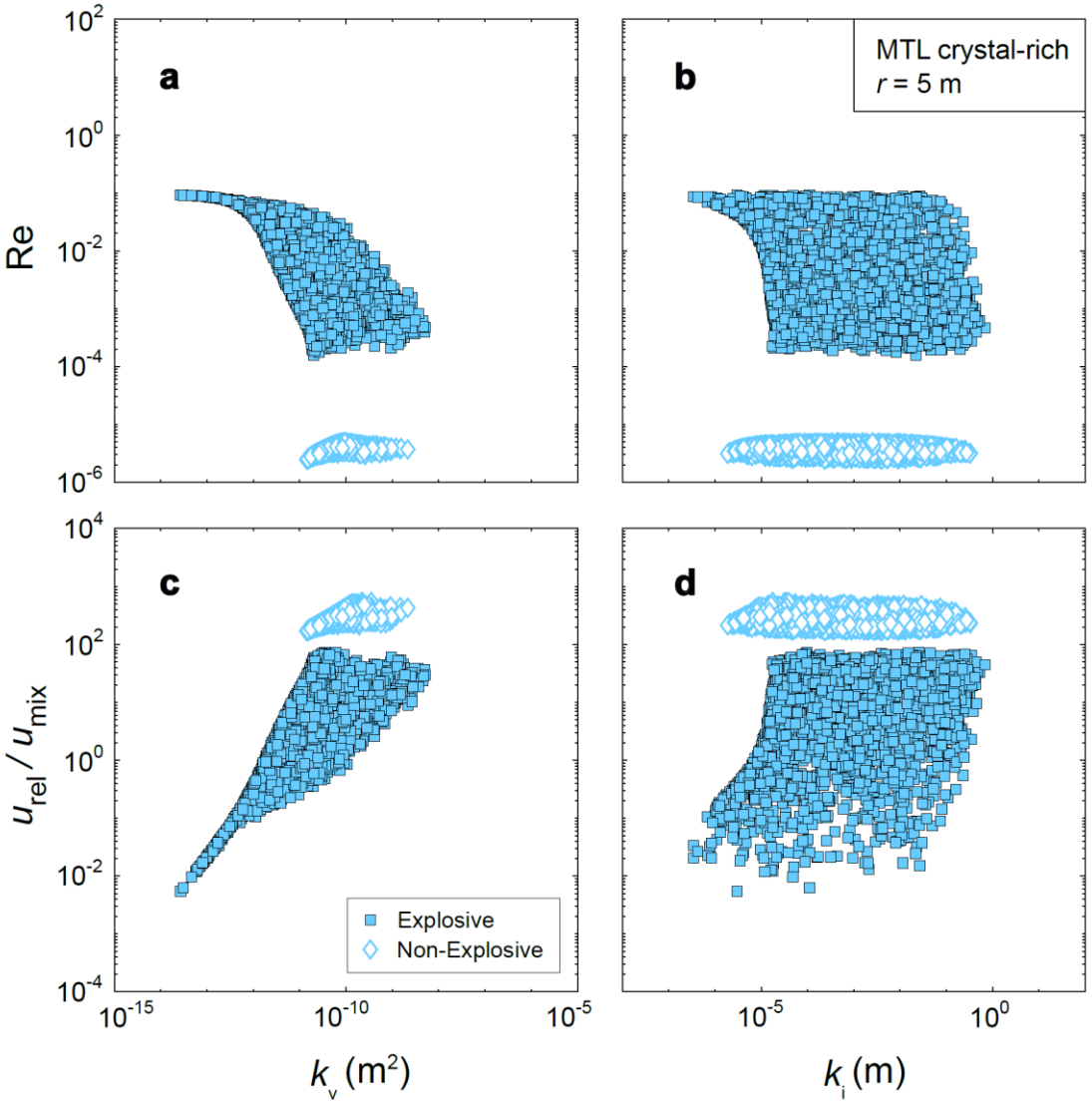

Supplementary Figure 7: Results of the sensitivity analysis using the MTL initial conditions and a conduit radius of 5 m, showing how the Reynolds number varies with **(a)** k_v and **(b)** k_i. Also shown is how u_{rel}/u_{mix} varies with **(c)** k_v and **(d)** k_i, where u_{rel} represents the relative velocity between the gas and melt phases and u_{mix} the velocity of the mixture. Each symbol represents a single solution.

Parameter	Variable	Reference Simulation			Unit
		MTL crystal-poor	MTL crystal-rich	Etna 122 BC	
Initial pressure	P	42	42	160	MPa
Initial temperature	T	1090	1070	1060	°C
Conduit radius	r	25	25	35	m
Conduit length	z	1600	1600	6000	m
Density (melt)	ρ_m	2700	2700	2700	kg m^{-3}
Dissolved H_2O	$x_{d_{H_2O}}$	2	2	3	wt. %
Dissolved CO_2	$x_{d_{CO_2}}$	457	457	4000	ppm
Initial crystal content (plg)	$\beta_{0_{plg}}$	5 [b]	10	5	vol. %
Initial crystal content (cpx)	$\beta_{0_{cpx}}$	3 [b]	5		vol. %
Initial crystal content (ol)	$\beta_{0_{ol}}$	2 [b]	2		vol. %
Characteristic time (crystallisation)	τ_c	10	10	10	s
Characteristic time (exsolution)	τ_e	10^{-5}	10^{-5}	10^{-5}	s

Supplementary Table 3: Initial conditions for the sensitivity analyses (excluding N_d, m, f_{tb} and f_0). Initial conditions for the MTL crystal-poor and crystal-rich endmembers are from Bamber et al.[6-7], whilst initial conditions for the Etna 122 BC sensitivity analysis are from Arzilli et al.[8] and La Spina et al.[9]. To account for the possibility that there is a higher initial volatile content for the Etna 122 BC eruption than measured in melt inclusions, a higher H_2O and CO_2 content was used for the Etna 122 BC simulations. The selected values for H_2O and CO_2 represent maximum values measured in melt inclusions from samples of the 2001 Etna flank eruption by Métrich et al.[10] and also represent equilibrium H_2O and CO_2 contents for the Etna composition at higher pressure, as determined by the H_2O-CO_2 solubility experiments of Allison et al.[11]. Therefore, although the H_2O and CO_2 contents are higher than the dissolved volatile contents measured by Del Carlo and Pompilo[12], the contents used in the simulations are likely more representative of the pre-eruptive condition and account for the possible exsolved volatile content at depth.

Supplementary Methods

1. *Synchrotron-based X-ray μCT: Additional sample information*

Our sample suite includes 10 vesicular scoria lapilli (Supplementary Table 1) from the Fontana Lapilli eruption (60 ka) of Las Sierras-Masaya volcanic system, Nicaragua. The Fontana Lapilli (FL) Plinian eruption ejected 2.9-3.8 km^3 of basaltic-andesitic tephra during the climatic phase, establishing an eruption column with an estimated maximum height of 32 km[1]. The Plinian phase had a mass eruption rate of 1.4 x 10^8 kg s^{-1}. The eruption has an estimated duration of 4-6 hours[1]. The eruption deposit is divided into 8 units from A-G (where final unit G is split into lower G and upper G), consisting of vesicular scoria lapilli, where there are no pauses in deposition. We use the classification of Costantini et al.[1] for the FL deposit, where the name 'FL_D' indicates that the sample was obtained from unit D. The sampling locality is that of Bamber et al.[7]. Units A-C belong to the opening stage of the FL eruption and were deposited by a moderately explosive phase with an unstable eruption column, culminating in the ash-rich unit C. Units D-LG belong to the main stage of the eruption and are a sequence of scoria lapilli with a massive internal structure dispersed over a wide area, indicating deposition by a sustained eruption column of Plinian intensity. The closing stage UG represents a return to an unstable eruption column[1].

Samples of the FL eruption are characterised by a distinctive micro-textural heterogeneity, where the crystal fraction can vary between 0.64 and 0.03, dominated by microlites and resulting in different vesicle morphologies[1,7]. This heterogeneity can either produce crystal-poor and crystal-rich scoriae, or can be found within the same scoria. Macroscale observations allow an approximate identification of these textural end members, as crystal-rich scoriae often have more irregular, sub-angular surface morphologies whilst crystal-poor scoriae are more fluidal in shape[1]. The samples examined in this study were selected to cover the eruption sequence from the opening (A/B) to the main (D-LG) stages and were visually inspected at the macroscale to select both the crystal-rich and crystal-poor endmembers, to examine how vesicularity changes over the course of the eruption and is influenced by conduit processes.

Our study also examines 6 vesicular scoria lapilli from the Masaya Triple Layer eruption (MTL) of Las Sierras-Masaya volcanic system. Compared to the FL eruption, the MTL eruption is more recent (2.1 ka) and the vent has been associated with the present-day

location of Masaya caldera, Nicaragua, a volcanic system which is active today[2]. The MTL eruption was a basaltic Plinian eruption, ejecting 3.4 km^3 of material and reaching a maximum eruption rate of 1 x 10^8 kg s^{-1} and maximum column height of 32 km [2]. The MTL eruption was a complex, episodic eruption occurring over weeks to months, with some stages representing phreatomagmatic activity[2]. Here we use the classification of Bamber et al.[6] to focus on the opening and Plinian stages of the MTL eruption, whilst removing stages which may be more representative of phreatomagmatic activity. Samples were selected from units TLL1, TLL2 and TLL3, where TLL1 represents the opening phase of the eruption and the latter units the main Plinian phases[6]. Similar to the FL eruption, samples of the MTL eruption are characterised by micro-textural heterogeneity, where crystal fraction can vary between 0.5 and 0.2 between microlite-rich and microlite-poor regions[6]. This textural heterogeneity also has an impact on vesicle textures within samples, so macroscale observations were also used to select samples which represent the crystal-rich and crystal-poor endmembers found in the MTL deposit.

The Etna 122 BC eruption was also a Plinian event, producing an erupted volume of 0.4 km^3 (estimated from exposed onshore deposits) of hawaiitic magma[3]. The mass eruption rate is estimated as 8.5 x 10^7 kg s^{-1}, whilst the maximum eruption column height is 26 km. The deposit is divided into 7 units[3], labelled A-G. Unit A was deposited by a less explosive event, producing a deposit with features typical of Strombolian eruptions, whilst B, D, F and G represent tuffs. Units C and E represent the Plinian phases of the eruption, depositing well-sorted scoria lapilli[3]. Samples of the Etna 122 BC eruption are highly crystalline, where the crystal fraction varies between 0.69-0.72 in crystalline clasts from Unit C, comprised dominantly of plagioclase, clinopyroxene and oxide microlites[13]. In our study we examine 2 samples of Unit C of the 122 BC eruption, to investigate the Plinian phase of the eruption.

The 2001 Etna flank eruption which occurred over a 2-month period between July and August erupted lava flows, lava fountains and Strombolian explosions from several eruptive fissures[14]. Our scoria sample represents a lava fountain from the lower vents, active during the 24-31 July period. Lava fountains produced at the end of July from the lower vents reached a maximum column height of 2 km. A total erupted tephra volume of 5-10 x 10^6 m^3 was produced by the eruption between July and August[15].

In contrast, the 23 November 2013 lava fountain was the most explosive episode occurring at Etna between 2011 and 2013. Within 45 minutes, 1.6 x 10^6 m^3 (DRE) of material had been

erupted, producing an eruption column height of 6 km [5]. The mass eruption rate[4] was estimated as 4.5 x 10^5 kg s^{-1} and the fallout deposit was reported at distances reaching 400 km away from the volcano. The 23 November 2013 lava fountain has been classified as a 'large-scale lava fountain' by Andronico et al.[16].

Crystal fraction (φ) was calculated for a clast of the 23 November 2013 lava fountain sample following the method of Hammer et al.[17]:

$$\varphi = \frac{A_x}{A}$$

Eq. 8

where A_x is the area of the phase of interest (x) and A the vesicle-free area of the sample.

2. *Synchrotron-based X-ray μCT: Image processing and analysis*

Here we provide further details on the image processing procedure and quantitative morphological and textural analysis. Samples were not cut into smaller volumes before acquisition, to preserve scoria morphology. For the majority of the samples, two contiguous sub-volumes were acquired.

First, a volume of interest (VOI) was selected, considering its representativeness for the sample. Most of the sample volumes were acquired as two separate sub-volumes, which were stitched to form a complete volume of approximately 6 mm^3. However, for some smaller scoriae or scoriae with a tapered morphology, one sub-volume or two smaller sub-volumes were acquired, corresponding to a volume smaller than 6 mm^3. To confirm that these larger and smaller volumes (e.g. MTL3_a0_1 and MTL3_a0_2) were both representative and allowed a direct comparison between two samples, the image analysis procedure was performed for a crystal-poor and a crystal-rich sample, with a volume of 6 mm^3 and a sub-volume of 3 mm^3. Porosity, connected porosity, tortuosity and the throat-pore size ratio were calculated for both volumes and the results compared. As the results for the 6 mm^3 and 3 mm^3 sized volumes were consistent, we suggest that 3 mm^3 is the minimum representative elementary volume (REV). An isotropic voxel size with an edge length of 0.9 μm was used for the tomographic reconstruction of all samples.

Following the stacking of images to produce complete sample volumes in ImageJ and after conversion to 8-bit raw format, image processing and analysis was completed using the commercial software Avizo (v. 2019.1; Thermo Fisher Scientific, USA). Firstly, for crystal-poor samples with spherical bubbles, filters were required to segment bubbles from the surrounding matrix glass. It was important to preserve thin glass films (<10 μm in thickness) during segmentation, due to the impact on connected porosity, as poor preservation of the films may lead to an apparent increase in connected porosity and, therefore, connectivity[18].

Edge-preserving filters were then applied, to preserve boundaries separating features of interest within the sample. First, the 3D *bilateral filter* available in Avizo was applied[19], using a kernel size of 9 (*x*, *y*, *z*) and a similarity of 20 in bilateral mode. Then, the 3D *non-local means filter*[20] was applied to the output of the bilateral filter, using a spatial standard deviation of 5 and an intensity standard deviation of 0.2. The search window was 10 voxels and the local neighbourhood considered 3 voxels. Filters were not applied to the crystal-rich samples of the Masaya Triple Layer and Etna 122 BC eruptions as both segmentation and preservation of the boundaries between vesicles did not require a pre-segmentation filtering process. Orthoslices of the 3D reconstructed volumes (Figure 1) were compared with representative 2D BSE images (Supplementary Figure 1) to examine vesicle morphologies and the influence of groundmass crystallinity. By comparing the 3D reconstructed volumes with 2D images, the representativeness of the analysed samples from the deposit and its textural characteristics were evaluated.

Sample porosity was determined as the volume of voxels comprising the pore space of a sample, with respect to the volume of voxels comprising the total sample volume. Instead, the connected porosity represents the volume of voxels comprising the connected pore space of a sample. Porosity and connected porosity were calculated using algorithms available in Avizo and the following steps. The *volume fraction* algorithm was used to calculate the volume of the pore space using the segmented binary images as the input. The *labeling* algorithm was then used on the binary images to identify connected pores within the sample. The *axis connectivity* algorithm was then applied using the output of the *labeling* algorithm, to produce an image containing all connected paths within the sample volume. Both *labeling* and *axis connectivity* considered a local neighbourhood of 26. The *volume fraction* algorithm was then used on the output of the *axis connectivity* algorithm to provide the volume of the connected pore space. Both porosity (Φ) and connected porosity (Φ_c) were calculated with respect to the total sample volume. The errors for porosity and connected porosity were assessed by

comparing the difference in the calculated values using two different thresholds for the segmentation of vesicles for the sample volume, with one threshold selected on the basis of its preservation of thin melt films separating vesicles and the second threshold selected which allowed greater segmentation of vesicles. The average error for porosity was ± 0.03 and the average error for connected porosity was ± 0.05.

To calculate vesicle number densities (N_d) and size distributions, connected vesicles needed to be separated. The *separate objects* algorithm in Avizo was used for this purpose, which separates objects using a marker-based watershed algorithm, combining a Chamfer distance map and H-maxima. The algorithm computes the watershed lines of a binary image. A marker extent of 8 was deemed most suitable for separating the smallest vesicles, whilst also preserving the volume of larger vesicles. An advantage of the watershed technique is that it preserves the original shape and volume of vesicles[21], an important consideration for calculating vesicle number densities and size distributions. The *label analysis* module was used to quantify the volume and number of individual vesicles in the sample volume, to produce bubble number densities (N_d). For the quantitative textural analysis of sample volumes, N_d was calculated as the number of bubbles per mm^3 of the total melt volume. However, $N_d{}^v$ was also calculated, representing the number of bubbles per mm^3 of the total sample volume, and is presented in Table 1 for comparison with N_d values. N_d values are preferentially used as the N_d is constant as bubbles grow[22-23].

To calculate sample tortuosity (τ), a skeleton was constructed for each sample using the *auto skeleton* algorithm in Avizo[24]. The algorithm computes a distance map of the segmented image, which is used to guide thinning and estimate the radii of fibres. A thinning procedure then uses the distance map to produce only a string of connected voxels, by removing voxels sequentially from the segmented object. The remaining voxel skeleton is then converted into a spatial graph object. The skeleton nodes represent bubbles, and the segments between nodes represent the pathways connecting these bubbles. The *auto skeleton* was applied to the output of the *axis connectivity* algorithm, to produce a skeleton of the connected porosity. Smoothing of the traced spatial graph was performed (10 iterations) with a smoothing coefficient of 0.5 and a value of 0.25 regarding the influence of the initial coordinate on its new position.

The skeletonization procedure provided the *x*, *y*, *z* spatial coordinates of the nodes and segments comprising the skeleton, with the node and segment IDs indicating which segments

connected which nodes (Supplementary Figure 8). The data obtained were processed using a custom MATLAB script (available in the Supplementary Information) to calculate the tortuosity for each segment connecting three nodes. Tortuosity (τ) was calculated as the length of two segments connecting three nodes/minimum length of the segment connecting two nodes as follows:

$$\tau = \frac{AB + BC}{AC}$$

Eq. 9

where *A*, *B* and *C* refer to individual nodes in which B is the middle node between A and C.

A minimum segment length was considered for the tortuosity calculation, due to the issue of multiple nodes being seeded within the same bubble by the skeletonization procedure[25]. This issue can create an unrealistically high number of nodes whilst producing very short segments, leading to spurious values of the tortuosity. Tortuosity was, therefore, only calculated for segments which exceeded the minimum length, determined from careful examination of textures in 3D sample volumes. Therefore, our approach allows us to calculate a local tortuosity. We then averaged the local tortuosity calculated for each set of segments to obtain a mean local tortuosity for the sample. Tortuosity was not calculated for samples FL_F_1 and MTL2_a0_2 as these samples have many small vesicles with very thin (<10 μm) pore-melt films, which are difficult to preserve during segmentation. As calculations of connectivity may therefore be overestimated for these samples, they were excluded from further analysis on the 3D connected pore network. The tortuosity and the tortuosity factor were computed for each set of segments. The mean and standard deviation (1σ) of τ and *m* are reported for each sample and are reported in Table 1 and Supplementary Data 2.

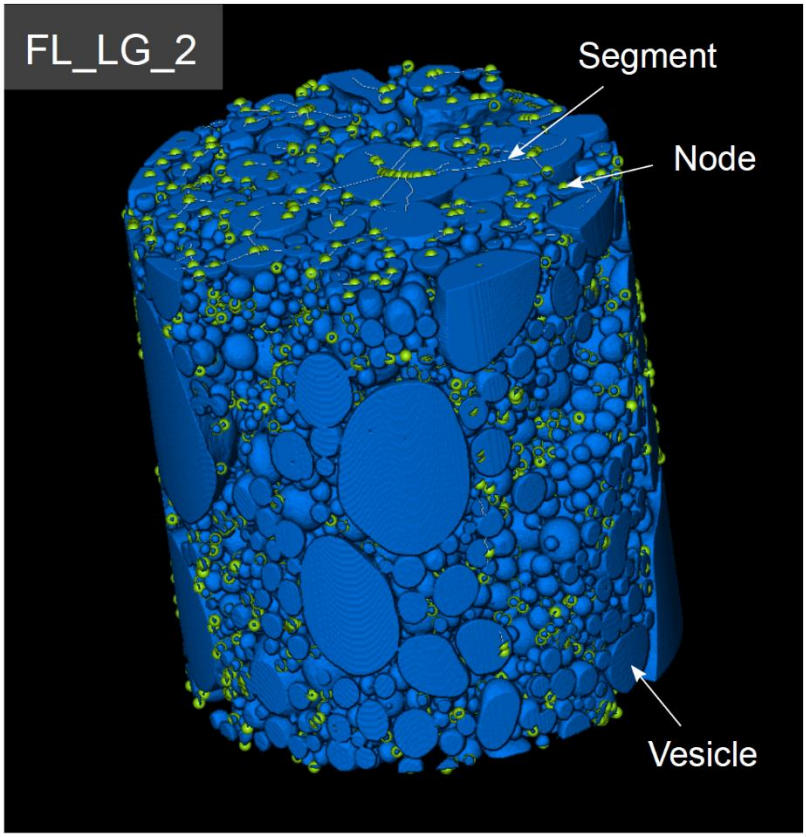

Supplementary Figure 8: Volume rendering of sample FL_LG_2, showing the skeletonization procedure used in Avizo, with nodes highlighted in green and the segments connecting two nodes highlighted by the white lines. Vesicles are also shown in blue.

To calculate the throat-pore ratio (f_{tb}), the *generate pore network model* algorithm was used in Avizo. The output of the *axis connectivity* procedure was used as the input file, as this is representative of the connected pore network. First, the *separate objects* module was applied in order to separate individual bubbles within the connected network. The pore network model produced a spatial graph, where endpoints of the network represent pores, and lines connecting the pores represent throats. The pore network model provided the *x*, *y*, *z* spatial coordinates of pores and throats and their radii, with their ID numbers indicating which pores are connected and by which throat. The radii of connected pores and throats were used in a custom MATLAB script (available in the Supplementary Information) to calculate the throat-pore size ratio as follows:

$$f_{\mathrm{tb}} = \frac{t_r}{mean_r}$$

Eq. 10

where $mean_r$ represents the average radii of the two connected pores, and t_r the radius of the throat which connects them. The f_{tb} was calculated for each throat-pore pair in the sample and is reported as a mean and standard deviation (1σ) for each sample.

3. *Simulations using the 1-Dimensional, steady-state conduit model*

Sensitivity analyses were performed using the 1D steady-state numerical conduit model of La Spina et al.[9,26-28]. This model simulates magma ascent within the conduit using a cylindrical geometry. In the model, the magma is considered as a two-phase mixture. Below the fragmentation level, this two-phase mixture is comprised of a liquid phase (containing melt, crystals, and dissolved volatiles) and the exsolved volatile phase. Instead, above the fragmentation level, the liquid phase is considered as a dispersed particle phase. The second phase continues to represent the exsolved volatiles above the fragmentation level. Both phases and their components are characterised by the volume fraction (α_k), mass density (ρ_k), mass fraction (x_k), velocity (u_k), specific internal energy (e_k), specific entropy (s_k), pressure (P_k) and temperature (T_k). The liquid phase is denoted using the index l (the dispersed particle phase above the fragmentation level), whilst the gas phase is denoted using the index g. Volatiles H_2O and CO_2 are represented by g_1 and g_2 respectively, whilst d_1 and d_2 are used to represent these volatile species as dissolved in the melt. The melt is represented by subscript m and the total crystal content by subscript c. The saturation constraints of $\alpha_l + \alpha_g = 1$ and $x_l + x_g = 1$ are maintained along the conduit. It is assumed that the components have the same pressure, temperature, and velocity within a single phase. Mixture parameters are defined as follows:

$$\rho = \alpha_l\rho_l + \alpha_g\rho_g; \qquad P = \alpha_l P_l + \alpha_g P_g;$$

$$x_l = \frac{\alpha_l\rho_l}{\rho}; \qquad T = \alpha_l T_l + \alpha_g T_g;$$

$$x_g = \frac{\alpha_g\rho_g}{\rho}; \qquad u = x_l u_l + x_g u_g;$$

$$e = x_l e_l + x_g e_g;$$

$$s = x_l s_l + x_g s_g.$$

Eq. 11

An equilibrium temperature between the gas and liquid phase is considered by the model, but the gas and liquid pressures and velocities can differ between each other[28]. The differences in pressure and velocity are controlled by the relaxation parameters, which are presented in further detail later.

Below we present the conservation equations for the mixture mass and momentum, following La Spina et al.[26-28]:

$$\frac{\partial \rho u}{\partial z} = 0,$$

Eq. 12

$$\frac{\partial}{\partial z}\left[\sum_{k=\mathrm{l,g}} \alpha_k \rho_k u_k^2 + \alpha_k P_k\right] = -\rho g - f_{\mathrm{D_l}} \frac{\rho_\mathrm{l} u_\mathrm{l}^2}{4r}(1 - \phi_\mathrm{f}) - f_{\mathrm{D_g}} \frac{\rho_\mathrm{g} u_\mathrm{g}^2}{4r}\phi_\mathrm{f},$$

Eq. 13

where g is the gravitational acceleration, r is the fixed conduit radius and ϕ_f is the fragmentation efficiency. The Darcy-Weisbach friction factors are represented by $f_{\mathrm{D_l}}$ and $f_{\mathrm{D_g}}$ and account for the friction with the wall of the conduit. These friction factors are functions of the Reynolds number and conduit wall roughness, as per the empirically derived Moody diagram[29-30].

In accordance with the formulation in Zein et al.[31] and Rodio and Abgrall[32], the mixture energy equation (including heat loss to gravitational force) is presented below:

$$\frac{\partial}{\partial z}\left[\sum_{k=\mathrm{l,g}} \alpha_k \rho_k u_k \left(e_k + \frac{P_k}{\rho_k} + \frac{u_k^2}{2}\right)\right] = -\rho g u.$$

Eq. 14

The balance equation described below accounts for the variation in liquid volume fraction, and consequently the gas volume fraction along the conduit:

$$\frac{\partial \rho u \alpha_\mathrm{l}}{\partial z} = -\frac{1}{\tau^{(\mathrm{p})}}\left(P_\mathrm{g} - P_\mathrm{l}\right).$$

Eq. 15

where the relaxation parameter $\tau^{(p)}$ ($m^2\ s^{-1}$) defines the disequilibrium between the gas and liquid pressures. We set $\tau^{(p)}$ to $10^{-8}\ m^2\ s^{-1}$, as we can assume equilibrium between the gas and liquid pressures due to the low viscosity of basaltic magma.

The following balance equations determine the exsolution of each gas component and the corresponding dissolved content in the melt:

$$\frac{\partial \alpha_{g_i} \rho_{g_i} u_g}{\partial z} = \frac{1}{\tau^{(e)}} \left(x_{d_i}^{md} - x_{d_i}^{md,eq} \right) \left(\alpha_l \rho_l - \sum_j \alpha_l \rho_{c_j} \beta_j \right),$$

Eq. 16

$$\frac{\partial}{\partial z} \left(\left(\alpha_l \rho_l - \sum_j \alpha_l \rho_{c_j} \beta_j \right) x_{d_i}^{md} u_l \right) = -\frac{1}{\tau^{(e)}} \left(x_{d_i}^{md} - x_{d_i}^{md,eq} \right) \left(\alpha_l \rho_l - \sum_j \alpha_l \rho_{c_j} \beta_j \right).$$

Eq. 17

where $x_{d_i}^{md}$ is the mass fraction of the dissolved gas phase *i* with respect to the liquid crystal-free phase and $x_{d_i}^{md,eq}$ is the same parameter but at equilibrium conditions. The rate of exsolution is controlled by the relaxation parameter $\tau^{(e)}$, which consequently controls how close the dissolved gas mass fraction is to the equilibrium value. We set $\tau^{(e)}$ to 10^{-5} s, assuming equilibrium, instantaneous exsolution.

The variation in crystal volume fraction (for each component) is defined as follows:

$$\frac{\partial}{\partial z} \left(\alpha_l \rho_{c_j} \beta_j u_l \right) = -\frac{1}{\tau^{(c)}} \alpha_l \rho_{c_j} \left(\beta_j - \beta_j^{eq} \right).$$

Eq. 18

where β_j is the volume fraction of crystal component *j* and β_j^{eq} the equilibrium volume fraction of the same component. The characteristic time $\tau^{(c)}$ (s) controls disequilibrium crystallisation and is defined below, following Arzilli et al.[8]:

$$\beta(t) = \beta^{eq} + \exp\left(-\frac{t}{\tau^{(c)}} \right) (\beta_0 - \beta^{eq})$$

Eq. 19

where β_0 is the initial crystal volume fraction and β^{eq} the equilibrium value. The rate of crystallisation is controlled by $\tau^{(c)}$. As we simulate the Masaya Triple Layer and Etna 122 BC Plinian eruptions, which are likely characterised by rapid syn-eruptive crystallisation of microlites[6,8] we set $\tau^{(c)}$ to 10 s, consistent with the experimental results of Arzilli et al.[8] on rapid crystallisation during the Etna 122 BC eruption.

The following differential equation describes the relative motion between the gas and liquid phases:

$$\frac{\partial}{\partial z}\left[\frac{u_{\mathrm{l}}^2}{2}-\frac{u_{\mathrm{g}}^2}{2}+e_{\mathrm{l}}+\frac{P_{\mathrm{l}}}{\rho_{\mathrm{l}}}-e_{\mathrm{g}}-\frac{P_{\mathrm{g}}}{\rho_{\mathrm{g}}}-\left(s_{\mathrm{l}}-s_{\mathrm{g}}\right)T\right]=$$

$$-\frac{1}{\tau^{(\mathrm{f})}}\frac{\rho}{\rho_{\mathrm{l}}\rho_{\mathrm{g}}}\left(u_{\mathrm{l}}-u_{\mathrm{g}}\right)-f_{\mathrm{D_l}}\frac{u_{\mathrm{l}}^2}{4\alpha_{\mathrm{l}}r}\left(1-\phi_{\mathrm{f}}\right)+f_{\mathrm{D_g}}\frac{u_{\mathrm{g}}^2}{4\alpha_{\mathrm{g}}r}\phi_{\mathrm{f}}\,.$$

Eq. 20

where the relaxation parameter $\tau^{(f)}$ (kg^{-1} m^3 s) controls the degree of decoupling between the phases. The degree of decoupling is greater for larger values of $\tau^{(f)}$. For small values of $\tau^{(f)}$, the relative velocity approaches zero, thereby maintaining coupling between the gas and liquid phases.

By setting the initial values of pressure, temperature H_2O, CO_2 and crystal content, the boundary condition at the inlet of the conduit can be defined. At the vent, two boundary conditions are possible depending on the result of the simulation, an atmospheric pressure condition and a choked flow condition. When the Mach number is equal to 1 and the mixture velocity is therefore equal to the speed of sound of the mixture, the choked flow condition results. The following equation describes the calculation of the speed of sound of the mixture:

$$C=\frac{1}{\sqrt{K_\rho}}$$

Eq. 21

where $K = \alpha_{\mathrm{l}}K_{\mathrm{l}} + \alpha_{\mathrm{g}}K_{\mathrm{g}}$ is the compressibility of the mixture.

A numerical solution is obtained using a shooting technique, where the initial magma ascent velocity is varied until one of the two boundary conditions at the vent is reached[33]. The step-size of integration is decreased automatically when the solution becomes highly non-linear.

The complex step derivative approximation described in La Spina et al.[34] is used to prevent the introduction of numerical errors as a result.

The governing equations described above present a general form of the numerical model, which can be applied to a wide range of volcanic systems and eruptive styles[9,26,28,35-36]. Therefore, constitutive equations are defined in order to apply the model to a specific volcanic system and regime, such as the Etna 122 BC and Masaya Triple Layer basaltic Plinian eruptions. The constitutive equations describing the rheological, solubility, outgassing, crystallisation, and fragmentation models, used to simulate the magma ascent dynamics of these volcanic systems are presented below. The equations of state are those described by La Spina et al.[26,37].

The following equation is used to model the viscosity of the liquid phase:

$$\mu_{\mathrm{l}} = \mu_{\mathrm{melt}} \cdot \theta_{\mathrm{c}} \cdot \theta_{\mathrm{b}},$$

Eq. 22

where μ_{melt} is the liquid phase viscosity, without crystals and bubbles. The factor θ_{c} accounts for the effect of crystals on magma viscosity[38], whilst the factor θ_{b} accounts for the effect of bubbles. The viscosity of the liquid phase is modelled using the model of Giordano et al.[39], which estimates μ_{melt} as a function of the melt composition, dissolved H_2O content and temperature:

$$\log(\mu_{\mathrm{melt}}) = A + \frac{B\left(y, x_{\mathrm{H_2O}}^{\mathrm{md}}\right)}{T - C\left(y, x_{\mathrm{H_2O}}^{\mathrm{md}}\right)}$$

Eq. 23

Parameter A is assumed as a constant for all melts and represents the logarithmic value of the viscosity at infinite temperature (A=-4.55). Instead, parameters B and C are functions of the melt composition (y) and the dissolved H_2O content ($x_{\mathrm{H_2O}}^{\mathrm{md}}$). For simulations of the Masaya Triple Layer eruption, the average melt inclusion composition of Bamber et al.[6] is used[7]. For simulations of the Etna 122 BC eruption, the average melt composition of Del Carlo and Pompilo[12] is used, consistent with Arzilli et al.[8]. The empirical model of Costa et al.[40] is used to model the increase of the viscosity of μ_1 due to crystallisation:

$$\theta = \frac{1 + \varphi^{\delta}}{[1 - F(\varphi, \xi, \gamma)]^{B\phi^*}}$$

Eq. 24

where

$$F = (1-\xi)\mathrm{erf}\left[\frac{\sqrt{\pi}}{2(1-\xi)}\varphi(1+\varphi^{\gamma})\right] \qquad \varphi = \frac{\left(\sum_{j=1}^{n_c} x_{c_j}^{l}\right)}{\phi^{*}}$$

Eq. 25

where the parameters of Vona et al.[41] are used for the fitting parameters B, δ, ξ, γ and ϕ^{*} and n_c represents the number of crystal components. The crystallisation model of Bamber et al.[7] was implemented in the sensitivity analyses performed for the Masaya Triple Layer eruption. Instead, the crystallisation model of Arzilli et al.[8] was implemented in the sensitivity analysis for the Etna 122 BC eruption.

To model the effect of bubbles on mixture viscosity, we follow Llewellin et al.[42]; Mader et al.[43] and La Spina et al.[36]. The effect of bubbles on mixture viscosity is controlled by the capillary number (*Ca*). This dimensionless number describes the ratio between the bubble relaxation time in response to deformation and the timescale of deformation in the fluid[43]. Consequently, bubbles tend to show spherical morphologies at low *Ca* and become more elongated with increasing *Ca.* As we observe few elongated bubbles in our reconstructed 3D sample volumes of the Fontana Lapilli and Masaya Triple eruptions, we model the effect of bubbles on the mixture viscosity[7] assuming $Ca << 1$. For the Etna 122 BC sensitivity analysis, we use the general formulation of Llewellin et al.[42], consistent with Arzilli et al.[8] and the more complex vesicle morphologies observed in the Etna samples.

The volatile solubility model considers H_2O and CO_2 as the two gas components (denoted with subscript *i*). A non-linear modification of Henry's Law is used to produce the equilibrium profile of the dissolved gas content $x_{d_i}^{md}$ as follows:

$$x_{d_i}^{md,eq} = \sigma_i \left(\frac{P_{g_i}}{\bar{P}}\right)^{\varepsilon_i}$$

Eq. 26

Where $P_{g_i} = \alpha_{g_i} P_g / \alpha_g$ is the partial pressure of the gas component *i* (Pa, $\bar{P}$ = 1 Pa is used to make the expression in the brackets adimensional) and α_g the volume fraction of the gas phase. Both the solubility coefficient σ_i and solubility exponent ε_i are assumed to be constant during magma ascent. We use the MagmaSat solubility model[44] to calculate the solubility

coefficients and solubility exponents, as this model provides the most appropriate calibration considering our magma compositions, and the pre-eruptive pressure and temperature conditions estimated for the eruptions[45]. For simulations of the Masaya Triple Layer eruption, we used the solubility coefficients (σ_{H_2O} = 8.3091 x 10^{-7}, σ_{CO_2} = 8.0193 x 10^{-12}) and solubility exponents (ε_{H_2O} = 0.5726, ε_{CO_2} = 0.988) using the average melt inclusion composition[6] and a temperature of 1100 ˚C[7]. For simulations of the Etna 122 BC eruption, we used the average melt inclusion composition[12] and a temperature of 1060 ˚C, producing the solubility coefficients σ_{H_2O} = 3.9257 x 10^{-7} and σ_{CO_2} = 3.9223 x 10^{-12} and the solubility exponents ε_{H_2O} = 0.6205 and ε_{CO_2} = 1.0269. All MagmaSat calculations were performed using VESIcal[45]. As we assume equilibrium exsolution, the dissolved volatile contents follow the equilibrium profile. The degree of decoupling is controlled by the relaxation parameter $\tau^{(f)}$, presented in the Methods as Equation 4.

To account for friction with the wall of the conduit during magma ascent, we model a friction parameter which evolves with the Reynolds number of ascent following La Spina et al.[36]. Hagen-Poiseuille's law is applied when the flow is laminar. When the flow becomes turbulent, the Colebrook equation[36,46] is used to approximate the friction factor.

As the conduit-wall friction is modelled considering both laminar and turbulent flow regimes, the Reynolds number (Re) of the liquid phase is calculated as follows:

$$\mathrm{Re} = \frac{\rho_l u_l 2r}{\mu_l}.$$

Eq. 27

As the density of the liquid (bubble-free) is approximately constant, the Reynolds number of ascent is directly dependent on the magma ascent velocity (magma ascent rate) and inversely proportional to the viscosity of the liquid. However, liquid viscosity also has an effect on the magma ascent velocity. Lower viscosity results in a higher magma ascent velocity, and thus a higher Reynolds number. Instead higher viscosity will lead to lower magma ascent velocity and a lower Reynolds number.

Hagen-Poiseuille's law is applied for laminar flow (Re < 2000) as follows:

$$f_{D_l}^{\mathrm{laminar}} = \frac{64}{\mathrm{Re}}.$$

Eq. 28

Instead for turbulent flow regimes (Re > 3000), the friction factor for fully developed turbulent flow is approximated following Fang et al.[46]:

$$f_{\mathrm{D_l}}^{\mathrm{turbulent}} = 1.613\left[\ln\left(0.23Rr^{1.1007} - \frac{60.525}{\mathrm{Re}^{1.1105}} + \frac{56.291}{\mathrm{Re}^{1.0712}}\right)\right]^{-2}.$$

Eq. 29

where *Rr* is the relative roughness of the pipe, assumed to be[36] *Rr* = 0.05. In the transitional regime ($2000 \leq \mathrm{Re} \leq 3000$), a linear interpolation between $f_{\mathrm{D_l}}^{\mathrm{laminar}}$ and $f_{\mathrm{D_l}}^{\mathrm{turbulent}}$ is used. Gas-wall drag ($f_{\mathrm{D_g}}$) is set to 0.03 above the fragmentation level, in accordance with Degruyter et al.[47].

Supplementary References

1. Costantini, L., Bonadonna, C., Houghton, B. & Wehrmann, H. New physical characterization of the Fontana Lapilli basaltic Plinian eruption, Nicaragua. *Bull. Volcanol.* **71,** 3, 337-355 (2009).
2. Pérez, W., Freundt, A., Kutterolf, S. & Schmincke, H.-U. The Masaya Triple Layer: A 2100 year old basaltic multi-episode Plinian eruption from the Masaya Caldera Complex (Nicaragua). *J. Volcanol. Geotherm. Res.* **179,** 191-205 (2009).
3. Coltelli, M., Del Carlo, P. & Vezzoli, L. Discovery of a Plinian basaltic eruption of Roman age at Etna volcano, Italy. *Geology*, **26,** 12, 1095-1098 (1998).
4. Andronico, D., Scollo, S. & Cristaldi, A. Unexpected hazards from tephra fallouts at Mt Etna: The 23 November 2013 lava fountain. *J. Volcanol. Geotherm. Res.* **304,** 118-125 (2015).
5. Bonaccorso, A., Calvari, S., Linde, A. & Sacks, S. Eruptive processes leading to the most explosive lava fountain at Etna volcano: The 23 November 2013 episode. *Geophys. Res. Lett.* **41,** 4912-4919 (2014).
6. Bamber, E.C. et al. Pre-and syn-eruptive conditions of a basaltic Plinian eruption at Masaya Volcano, Nicaragua. *J. Volcanol. Geotherm. Res.* **392,** 106761 (2020).
7. Bamber, E.C. et al. Basaltic Plinian eruptions at Las Sierras-Masaya volcano driven by cool storage of crystal-rich magmas. *Commun. Earth Environ.* **3,** 253 (2022).
8. Arzilli, F. et al. Magma fragmentation in highly explosive basaltic eruptions induced by rapid crystallization. *Nat. Geosci.* **12,** 1023-1028 (2019).
9. La Spina, G., Arzilli, F., Burton, M.R., Polacci, M. & Clarke, A.B. (2022). Role of volatiles in highly explosive basaltic eruptions. *Commun. Earth Environ.* **3,** 156 (2022).
10. Métrich, N., Allard, P., Spilliaert, N., Andronico, D. & Burton, M. 2001 flank eruption of the alkali- and volatile-rich primitive basalt responsible for Mount Etna's evolution in the last three decades. *Earth Planet. Sci. Lett.* **228,** 1-17 (2004).
11. Allison, C.M., Roggensack, K. & Clarke, A.B. H_2O-CO_2 solubility in alkali-rich mafic magmas: new experiments at mid-crustal pressures. *Contrib. Mineral. Petrol.* **174,** 58 (2019).
12. Del Carlo, P. & Pompilo, M. The relationship between volatile content and the eruptive style of basaltic magma: the Etna case. *Ann. Geophys.* **47,** 4, 1423-1432 (2004).

13. Sable, J., Houghton, B., Del Carlo, P. & Coltelli, M. Changing conditions of magma ascent and fragmentation during the Etna 122 BC basaltic Plinian eruption: Evidence from clast microtextures. *J. Volcanol. Geotherm. Res.* **158,** 3-4, 333-354 (2006).
14. Taddeucci, J., Pompilio, M. & Scarlato, P. Monitoring the explosive activity of the July-August 2001 eruption of Mt. Etna (Italy) by ash characterization. *Geophys. Res. Lett.* **29,** 8, 1230 (2002).
15. Behncke, B. & Neri, M. The July-August 2001 eruption of Mt. Etna (Sicily). *Bull. Volcanol.* **65,** 7, 461-476 (2003).
16. Andronico, D., Cannata, A., Di Grazia, G. & Ferrari, F. The 1986-2021 paroxysmal episodes at the summit craters of Mt. Etna: Insights into volcano dynamics and hazard. *Earth Sci. Rev.* **220,** 103686 (2021).
17. Hammer, J.E., Cashman, K.V., Hoblitt, R.P. & Newman, S. Degassing and microlite crystallization during pre-climatic events of the 1991 eruption of Mt. Pinatubo, Philippines. *Bull Volcanol.* **60,** 355-380 (1999).
18. Shea, T. et al. Textural studies of vesicles in volcanic rocks: An integrated methodology. *J. Volcanol. Geotherm. Res.* **190,** 3-4, 271-289 (2010).
19. Tomasi, C. & Manduchi, R. Bilateral Filtering for Gray and Color Images. *Sixth international conference on computer vision (IEEE Cat. No. 98CH36271)*, IEEE, 839-846 (1998).
20. Gastal, E.S.L. & Oliveira, M.M. Adaptive manifolds for real-time high-dimensional filtering. *ACM Trans. Graph.* **31,** 4, 1-13 (2012).
21. Liedl, A. et al. A 3D imaging textural characterization of pyroclastic products from the 1538 AD Monte Nuovo eruption (Campi Flegrei, Italy). *Lithos* **340-341,** 316-331 (2019).
22. Le Gall, N. & Pichavant, M. Homogeneous bubble nucleation in H_2O- and H_2O-CO_2-bearing basaltic melts: Results of high temperature decompression experiments. *J. Volcanol. Geotherm. Res.* **327,** 604-621 (2016).
23. Proussevitch, A.A., Sahagian, D.L. & Carlson, W.D. Statistical analysis of bubble and crystal size distributions: Application to Colorado Plateau basalts. *J. Volcanol. Geotherm. Res.* **164,** 3, 112-126 (2007).
24. Fouard, C., Malandain, G., Prohaska, S. & Westerhoff, M. Blockwise processing applied to brain microvascular network study. *IEEE Trans. Med. Imaging* **25,** 10, 1319-1328 (2006).

25. Lindquist, W.B., Lee, S.M., Coker, D.A., Jones, K.W. & Spanne, P. Medial axis analysis of void structure in three-dimensional tomographic images of porous media. *J. Geophys. Res. Solid Earth* **101,** B4, 8297-8310 (1996).
26. La Spina, G., Burton, M. & de' Michieli Vitturi, M. Temperature evolution during magma ascent in basaltic effusive eruptions: A numerical application to Stromboli volcano. *Earth Planet. Sci. Lett.* **426,** 89-100 (2015).
27. La Spina, G., Polacci, M., Burton, M. & de' Michieli Vitturi, M. Numerical investigation of permeability models for low viscosity magmas: Application to the 2007 Stromboli effusive eruption. *Earth Planet. Sci. Lett.* **473,** 279-290 (2017a).
28. La Spina, G. et al. Explosivity of basaltic lava fountains is controlled by magma rheology, ascent rate and outgassing. *Earth Planet. Sci. Lett.* **553,** 116658 (2021).
29. Weisbach, J.L. *Lehrbuch der Ingenieur- und Maschinen-Mechanik: ohne Anwendung des höhern Calculs für den Unterricht an technischen Lehranstalten sowie zum Gebrauche für Techniker: in zwei Theilen*. Theoretische Mechanik, Viewig (1845).
30. Brown, G.O. The history of the Darcy-Weisbach equation for pipe flow resistance. *In: Environmental and Water Resources History*, 34-45 (2003).
31. Zein, A., Hantke, M. & Warnecke, G. Modeling phase transition for compressible two-phase flows applied to metastable liquids. *J. Comput. Phys.* **229,** 2964-2998 (2010).
32. Rodio, M.G. & Abgrall, R. An innovative phase transition modelling for reproducing cavitation through a five-equation model and theoretical generalization to six and seven-equation models. *Int. J. Heat Mass Transf.* **89,** 1386-1401 (2015).
33. de' Michieli Vitturi, M., Clarke, A. B., Neri, A. & Voight, B. Effects of conduit geometry on magma ascent dynamics in dome-forming eruptions. *Earth Planet. Sci. Lett.* **272,** 3-4, 567-578 (2008).
34. La Spina, G., de' Michieli Vitturi, M. & Clarke, A.B. Transient numerical model of magma ascent dynamics: application to the explosive eruptions as the Soufrière Hills Volcano. *J. Volcanol. Geotherm. Res.* **336,** 118-139 (2017b).
35. La Spina, G., Burton, M., de'Michieli Vitturi, M. & Arzilli, F. Role of syn-eruptive plagioclase disequilibrium crystallization in basaltic magma ascent dynamics. *Nat. Commun.* **7,** 13402 (2016).
36. La Spina, G. et al. Conduit dynamics of highly explosive basaltic eruptions: The 1085 CE Sunset Crater sub-Plinian events. *J. Volcanol. Geotherm. Res.* **387,** 106658 (2019).

37. La Spina, G., de' Michieli Vitturi, M. & Romenski, E. A compressible single-temperature conservative two-phase model with phase transitions. *Int. J. Numer. Methods Fluids* **76,** 282-311 (2014).
38. Costa, A. Viscosity of high crystal content melts: Dependence on solid fraction. *Geophys. Res. Lett.* **32,** 22 (2005).
39. Giordano, D., Russell, J. & Dingwell, D. Viscosity of magmatic liquids: A model. *Earth Planet. Sci. Lett.* **271,** 1-4, 123-134 (2008).
40. Costa, A., Caricchi, L. & Bagdassarov, N. A model for the rheology of particle-bearing suspensions and partially molten rocks. *Geochem. Geophys. Geosyst*. **10,** 3 (2009).
41. Vona, A., Romano, C., Dingwell, D.B. & Giordano, D. The rheology of crystal-bearing basaltic magmas from Stromboli and Etna. *Geochim. Cosmochim. Acta* **75,** 3214-3216 (2011).
42. Llewellin, E.W., Mader, H.M. & Wilson, S.D.R. The constitutive equation and flow dynamics of bubbly magmas. *Geophys. Res. Lett.* **29,** 24 (2002).
43. Mader, H.M., Llewellin, E.W. & Mueller, S.P. The rheology of two-phase magmas: A review and analysis. *J. Volcanol. Geotherm. Res.* **257,** 135-158 (2013).
44. Ghiorso, M.S. & Gualda, G.A.R. An H_2O-CO_2 mixed fluid saturation model compatible with rhyolite-MELTS. *Contrib. Mineral. Petrol.* **169,** 6, 1-30 (2015).
45. Iacovino, K., Matthews, S., Wieser, P.E., Moore, G.M. & Bégué, F. VESIcal part I: An open-source thermodynamic model engine for mixed volatile (H_2O-CO_2) solubility in silicate melts. *Earth Space Sci.* **8,** e2020EA001584 (2021).
46. Fang, X., Xu, Y. & Zhou, Z. New correlations of single-phase friction factor for turbulent pipe flow and evaluation of existing single-phase friction factor correlations. *Nucl. Eng. Des.* **241,** 3, 897-902 (2011).
47. Degruyter, W., Bachmann, O., Burgisser, A. & Manga, M. The effects of outgassing on the transition between effusive and explosive silicic eruptions. *Earth Planet. Sci. Lett.* **349-350,** 161-170 (2012).